

PAPER • OPEN ACCESS

Effect of Cu substitution on anion redox behaviour in P3-type sodium manganese oxides

To cite this article: Stephanie F Linnell *et al* 2022 *J. Phys. Energy* 4 044006

View the [article online](#) for updates and enhancements.

You may also like

- [Review on anionic redox for high-capacity lithium- and sodium-ion batteries](#)
Chenglong Zhao, Qidi Wang, Yaxiang Lu et al.
- [THE CO-TO-H₂ CONVERSION FACTOR ACROSS THE PERSEUS MOLECULAR CLOUD](#)
Min-Young Lee, Snežana Stanimirovi, Mark G. Wolfire et al.
- [Review—Research Progress on Layered Transition Metal Oxide Cathode Materials for Sodium Ion Batteries](#)
Fanglin Wei, Qiaoping Zhang, Peng Zhang et al.



PAPER

OPEN ACCESS

Effect of Cu substitution on anion redox behaviour in P3-type sodium manganese oxides

RECEIVED
29 July 2022REVISED
16 September 2022ACCEPTED FOR PUBLICATION
28 September 2022PUBLISHED
12 October 2022

Original content from this work may be used under the terms of the [Creative Commons Attribution 4.0 licence](#).

Any further distribution of this work must maintain attribution to the author(s) and the title of the work, journal citation and DOI.

Stephanie F Linnell^{1,2} , Alexis G Manche^{1,2} , Yingling Liao^{1,2}, Moritz Hirsbrunner³ , Saki Imada⁴, Aaron B Naden² , John T S Irvine^{1,2} , Laurent C Duda³ and A Robert Armstrong^{1,2,*} ¹ School of Chemistry, University of St Andrews, St Andrews, Fife KY16 9ST, United Kingdom² The Faraday Institution, Quad One, Harwell Science and Innovation Campus, Didcot OX11 0RA, United Kingdom³ Department of Physics and Astronomy, Division of X-ray Photon Science, Uppsala University, Uppsala S-75120, Sweden⁴ Faculty of Electrical Engineering and Electronics, Kyoto Institute of Technology, Sakyo, Kyoto 606-8585, Japan

* Author to whom any correspondence should be addressed.

E-mail: ara@st-andrews.ac.uk**Keywords:** sodium-ion batteries, cathode materials, layered oxides, anion redoxSupplementary material for this article is available [online](#)**Abstract**

Sodium layered oxides which display oxygen anion redox behaviour are considered promising positive electrodes for sodium-ion batteries because they offer increased specific capacities. However, they suffer from irreversible structural changes resulting in significant capacity loss and limited oxygen redox reversibility. Here the effect of Cu substitution on the electrochemical performance of P3-type sodium manganese oxide is examined by evaluating the structural and electronic structural evolution upon cycling, supported by density functional theory (DFT) calculations. Over the voltage range 1.8–3.8 V vs. Na/Na⁺, where the redox reactions of the transition metal ions contribute entirely towards the charge compensation mechanism, stable cycling performance is maintained, showing a capacity retention of 90% of the initial discharge capacity of 166 mA h g⁻¹ after 40 cycles at 10 mA g⁻¹. Over an extended voltage range of 1.8–4.3 V vs. Na/Na⁺, oxygen anion redox is invoked, with a voltage hysteresis of 110 mV and a greater initial discharge capacity of 195 mA h g⁻¹ at 10 mA g⁻¹ is reached. Ex-situ powder x-ray diffraction patterns reveal distortion of the P3 structure to P'3 after charge to 4.3 V, and then transformation to O'3 upon discharge to 1.8 V, which contributes towards the capacity fade observed between the voltage range 1.8–4.3 V. DFT with projected density of states calculations reveal a strong covalency between the copper and oxygen atoms which facilitate both the cationic and anionic redox reactions in P3-type Na_{0.67}Mn_{0.9}Cu_{0.1}O₂.

1. Introduction

Sodium-ion batteries (SIBs) are attractive alternatives to lithium-ion batteries especially for large-scale applications, on account of safety, high-abundance, low-cost and uniform geographical distribution of sodium [1–4]. This is particularly true for grid energy storage devices where cost, abundant resource supply and safety are important factors. For the practical application of SIBs, high energy density positive electrodes are required [4–7]. Consequently, great efforts have been dedicated to developing positive electrode materials for SIBs. Among the materials studied, manganese-based sodium layered oxides, Na_xM_yO₂ (M = transition metal) are an attractive family for SIBs [8–14]. These layered oxides can be classified into three polymorphs O3, P2 and P3, according to the oxygen stacking sequence and the coordination environments of Na⁺ ions which can be either octahedral (O) or trigonal prismatic (P), as described by Delmas *et al* [15]. These materials can deliver high capacities, which may be enhanced by exploiting both cation and anionic redox reactions to increase the energy density. However, the reversibility of oxygen anion redox reactions are limited and influenced by cation ordering of the transition metal layer, cation migration and lattice oxygen loss [16]. To enhance the performance of oxygen anion redox, it is important to stabilise labile oxygen and suppress

irreversible structural changes. Partial substitution of Mn by Ni²⁺, Zn²⁺, and Cu²⁺ and/or the presence of transition metal vacancies promote reversible oxygen redox whilst maintaining structural stability and suppressing voltage hysteresis [17–26]. For instance, Kim *et al* reported a high initial discharge capacity of 204 mA h g⁻¹ for P3-Na_{0.67}Mn_{0.8}Ni_{0.2}O₂, of which the Mn³⁺/Mn⁴⁺, Ni²⁺/Ni³⁺/Ni⁴⁺ and O²⁻/(O₂)ⁿ⁻ redox couples contributed toward the charge mechanism, as evidenced by x-ray absorption spectroscopy (XAS) and resonant inelastic x-ray spectroscopy (RIXS). These data also showed that the presence of Ni facilitated the electron transfer between O 2p and the transition metal 3d bands because of the strong Ni 3d-O 2p hybridisation which stabilised the oxygen redox activity by a reductive coupling mechanism [17].

Manganese-based sodium layered oxides doped with Cu²⁺ have also attracted attention as potential positive electrode materials for SIBs since the Cu²⁺/Cu³⁺ redox couple can provide additional capacity, raise the redox potential and due to their potential low cost and safety advantages compared to Ni- and Co-doped materials [24, 25, 27–30]. Zheng *et al* synthesised the P2-type Na_{0.67}Cu_{0.28}Mn_{0.72}O₂ material which delivered a discharge capacity of 84 mA h g⁻¹ at 1.0 C over the voltage range 2.0–4.5 V with a capacity retention of 98% over 50 cycles, exceeding the cycling stability of most other P2-type materials over the high-voltage region [24]. Structural analysis revealed that the P2-structure and oxygen stacking was maintained upon cycling, resulting in a suppressed voltage hysteresis of 160 mV for the oxygen redox reaction [24]. Wang *et al* studied the P2-type Na_{2/3}Mn_{0.72}Cu_{0.22}Mg_{0.06}O₂ material, and reported a reversible capacity of 107.6 mA h g⁻¹ between 2.0 and 4.5 V, with a capacity retention of 87.9% over 100 cycles. This material exhibited solid-solution behaviour on cycling based on *in-situ* powder x-ray diffraction (PXRD) and XAS data revealed a charge compensation mechanism based on the Mn³⁺/Mn⁴⁺, Cu²⁺/Cu³⁺ and O²⁻/(O₂)ⁿ⁻ redox couples [27].

These previous studies have focused on Cu-substituted P2-type sodium layered manganese oxides, even though P3-type materials may be considered more sustainable since they can form at lower temperatures. Additionally, P2- and P3-type materials can present different electrochemical performance as a result of the differences in the oxygen stacking of these polymorphs. Therefore, to understand the oxygen redox activity in P3-type Na_xMn_{1-y}M_yO₂ (M = transition metal, x = 0.67, 0.1 ≤ y ≤ 0.2) materials, we have studied the effects of Cu-doping in P3-type Na_{0.67}Mn_{0.9}Cu_{0.1}O₂. The structural and electronic structural evolution of P3-type Na_{0.67}Mn_{0.9}Cu_{0.1}O₂ over the first cycle in the voltage ranges 1.8–3.8 V and 1.8–4.3 V were thoroughly investigated using a range of spectroscopic methods and PXRD. Over the voltage range 1.8–4.3 V, P3-Na_{0.67}Mn_{0.9}Cu_{0.1}O₂ exhibits oxygen anion redox activity and density functional theory (DFT) calculations demonstrate that such oxygen anion redox activity is associated with the existence of a weak Cu–O bond near the Fermi Level.

2. Experimental

2.1. Materials synthesis

Two solutions were prepared, the first a stoichiometric amount of sodium carbonate (Na₂CO₃, Fischer Chemistry, ≥99.5%), the second a stoichiometric mixture of manganese(II) acetate tetrahydrate (Mn(CH₃CO₂)₂·4H₂O, Aldrich, ≥99%) and copper acetate monohydrate (Cu(CH₃CO₂)₂·H₂O, Acros Organics, 98+%). The first solution was added dropwise, while stirring to the second solution, and the mixture stirred for a further 10 min. A rotary evaporator was used to remove the water and the resulting powder heated to 300 °C at a rate of 5 °C min⁻¹ for 12 h, and then ground using a pestle and mortar. The powder was pelletised and heated to 625 °C at a rate of 5 °C min⁻¹ for 1 h under air and then quenched. As-synthesised Na_{0.67}Mn_{0.9}Cu_{0.1}O₂ was stored in an argon filled glovebox.

2.2. Materials characterisation

For structural analysis, PXRD patterns of as-synthesised Na_{0.67}Mn_{0.9}Cu_{0.1}O₂ and ex-situ samples were measured using a PANanalytical Empyrean diffractometer, using Mo-Kα_{1,2} radiation (λ = 0.7107 Å) with a Zr β filter and X'celerator detector. Diffraction data were collected at room temperature within the 2θ range 5.0–40.0° over 24 h per scan, with a step size of 0.0084°, 4189 steps and a time per step of 20.6 s, in 0.7 mm capillaries. For ex-situ PXRD patterns, 80 wt% of active material was mixed with 20 wt% super C65 carbon in an argon filled glovebox for 15 m. Swagelok cells were prepared in an argon filled glovebox which were made up of a positive electrode (typical mass loading of ~30 mg cm⁻²), a sodium metal disc negative electrode separated by glass fibre separators (Whatman, GF/F) saturated with electrolyte (1M NaPF₆ in ethylene carbonate/diethyl carbonate (1:1 v/v%), Kishida). Swagelok cells were cycled galvanostatically to different states of charge/discharge at a current rate of 10 mA g⁻¹ using a Biologic MacPile II system at 30 °C. The electrodes were extracted post-cycling, washed with dry dimethyl carbonate (DMC, Sigma Aldrich, ≥99%) three times in an argon filled glovebox and vacuum dried. PXRD data were analysed using the Rietveld method using Topas Academic V6 [31]. To examine the morphology and elemental distribution

of as-synthesised $\text{Na}_{0.67}\text{Mn}_{0.9}\text{Cu}_{0.1}\text{O}_2$, a Schottky field-emission gun scanning electron microscope (SEM, FEI Scios dualbeam) equipped with an EDAX Octane Plus EDS detector was employed.

Ex-situ Mn and Cu L-edge, and O K-edge soft x-ray absorption spectroscopy (SXAS) and resonant inelastic x-ray scattering (RIXS) spectra were obtained at the beamline BL27SU at Spring 8, Japan [32]. CR2325 coin cells were assembled as described below using Solupor membrane as separator. After cycling, electrodes were recovered, rinsed with DMC three times and vacuum dried. SXAS and RIXS data were collected at the Mn and Cu L-edge and O K-edge, partial fluorescence yield (PFY) and total electron yield (TEY) signals were measured simultaneously at a resolution of about 0.1 eV. PFY was detected using an energy dispersive soft x-ray analyser and TEY was recorded using the sample drain current detected by a pico-ammeter. Oxygen K-edge RIXS spectra were recorded with a spectrometer of a varied-line-spacing plane cylindrical grating design in first order of diffraction at a combined resolution of about 0.4 eV. The vertical (horizontal) beam size at sample point is about 10 μm (200 μm).

2.3. Electrochemical measurements

To study the electrochemical properties, positive electrodes were made by mixing 75 wt% of $\text{Na}_{0.67}\text{Mn}_{0.9}\text{Cu}_{0.1}\text{O}_2$, with 15 wt% super C65 carbon and 10 wt% Solef binder (modified polyvinylidene fluoride) in n-methyl-2-polyvinylidene, in air. The slurry was cast onto aluminium foil and 13 mm diameter discs were punched out and vacuum dried at 80 °C, giving an average electrode loading of 2.6 mg cm^{-2} . CR2325 coin cells were assembled in an argon filled glovebox, made up of a positive disc electrode and metallic sodium as the counter/reference electrode, separated by a glass fibre separator (Whatman, GF/F) soaked in electrolyte, 1M NaPF_6 in ethylene carbonate/diethyl carbonate (1:1 v/v%), Kishida). Cells were cycled in galvanostatic and potentiostatic (linear sweep voltammetry) mode in a temperature-controlled environment at 30 °C using a Biologic BCS-805 battery cycler.

2.4. Theoretical simulation

Electronic properties were analysed by DFT calculations as implemented in the Vienna *Ab initio* Simulation Package code with Perdew–Burke–Ernzerhof functional form of the generalised-gradient approximation and projector augmented wave pseudo-potentials [33]. An energy cut-off of 520 eV was applied as well as an effective U (Hubbard) correction of 4.0 eV for Mn 3*d*-electrons and 3.9 eV for Cu 3*d*-electrons to remove fractional occupancies in those orbitals. A k-points grid of 4 × 6 × 2 was used for geometry optimisation and a larger k-points grid 6 × 9 × 3 to obtain the projected density of states (pDOSs). The convergence threshold was set to 10⁻⁵ in energy with 0.01 eV Å⁻¹ in force. Bader charges were calculated to understand the charge repartition between the different Mn sites within the structure [34].

3. Results and discussion

3.1. Characterisation of $\text{Na}_{0.67}\text{Mn}_{0.9}\text{Cu}_{0.1}\text{O}_2$

The PXRD pattern of $\text{Na}_{0.67}\text{Mn}_{0.9}\text{Cu}_{0.1}\text{O}_2$ can be indexed to an ideal P3 structure, except for trace amounts of CuO as highlighted in figure S1. The major diffraction peaks are well-fitted by Rietveld refinement using the P3-type structural model with space group, *R3m* for as-synthesised $\text{Na}_{0.67}\text{Mn}_{0.9}\text{Cu}_{0.1}\text{O}_2$. The profile fit is shown in figure 1(a) and the results of the Rietveld refinement are detailed in table 1. The occupancies of the transition metals and sodium were refined, and these results reveal the composition of the as-synthesised material to be $\text{Na}_{0.69}\text{Mn}_{0.9}^{+3.46}\text{Cu}_{0.1}\text{O}_2$. This structure can be described as consisting of layers of edge-sharing MO_6 (*M* = transition metal) octahedra and Na^+ ions which occupy trigonal prismatic sites, with an ABCCA oxygen stacking sequence, illustrated in figure 1(b). A SEM micrograph, representative of as-synthesised $\text{Na}_{0.67}\text{Mn}_{0.9}\text{Cu}_{0.1}\text{O}_2$, is shown figure 1(c). This reveals that the sample has a uniform morphology made up of agglomerated primary particles, roughly 100 nm in size. EDS elemental maps for $\text{Na}_{0.67}\text{Mn}_{0.9}\text{Cu}_{0.1}\text{O}_2$ are shown in figure 1(d). These maps show even distribution of Na, Mg, Cu, and O. Furthermore, the stoichiometry of Mn and Cu (normalised to Mn + Cu = 1.0) was determined to be 0.89 and 0.11, respectively, by EDS analysis averaged across numerous regions.

As we have seen previously from the structure refinement, the average charge on the Mn sites is around $\sim +3.5$. Thus, to help determine if there is a possible charge separation between the different Mn sites and therefore check if some favour a +4 charge and others a +3 charge, Bader analysis was performed. The results suggest that there are two types of Mn site for which the average calculated charges are different. The first type of site has an average charge of around $\sim +3.7$ and thus will be better able to accommodate Mn^{4+} , and a second site with an average charge of $\sim +3.4$ which will be more favourable for the Mn^{3+} . Figure 2 shows the distribution of these different Mn sites in the BC and AB layers. In the BC layer hosting the Cu sites, we note that there is a greater presence of Mn with an average charge of +3.7 and that therefore more Mn^{4+} will have to be present on this face. The charge on the Cu being lower (+2), the greater presence of Mn^{4+} here

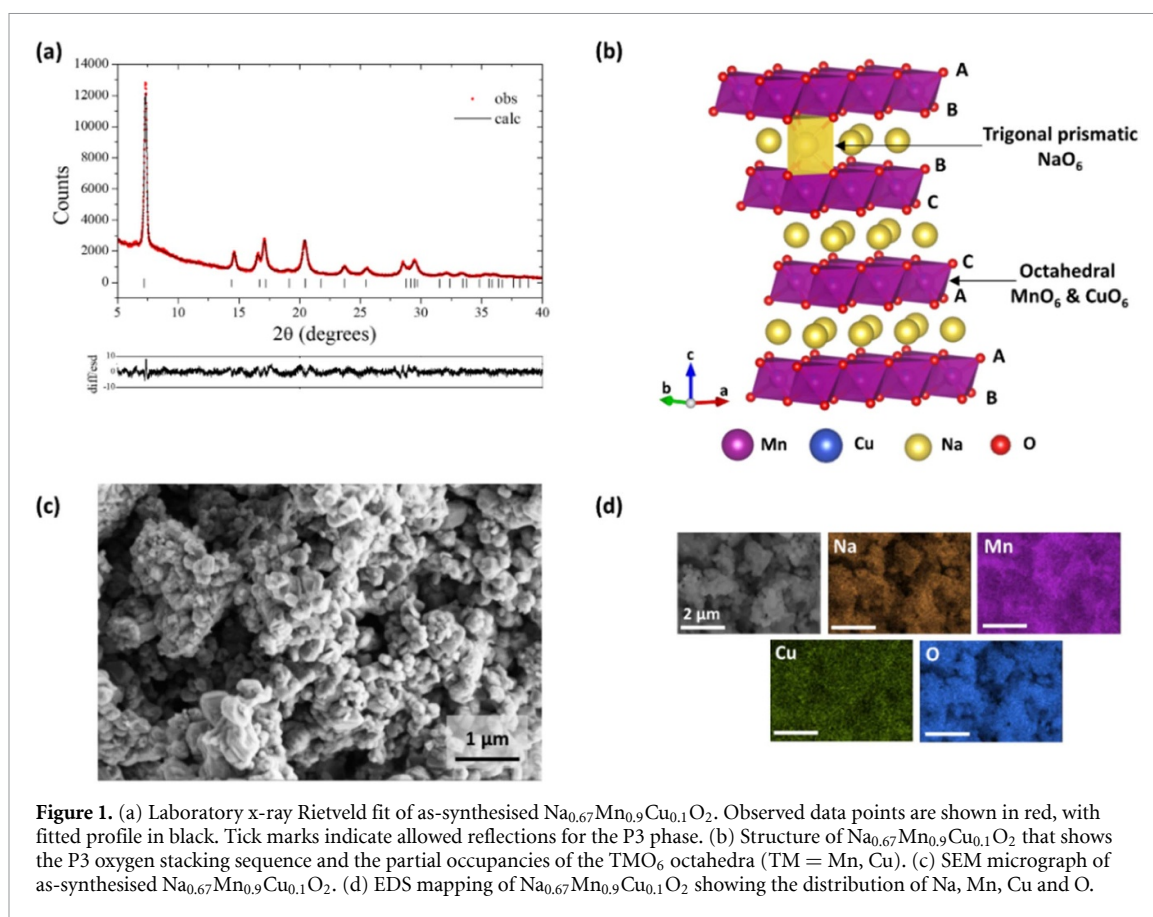


Figure 1. (a) Laboratory x-ray Rietveld fit of as-synthesised $\text{Na}_{0.67}\text{Mn}_{0.9}\text{Cu}_{0.1}\text{O}_2$. Observed data points are shown in red, with fitted profile in black. Tick marks indicate allowed reflections for the P3 phase. (b) Structure of $\text{Na}_{0.67}\text{Mn}_{0.9}\text{Cu}_{0.1}\text{O}_2$ that shows the P3 oxygen stacking sequence and the partial occupancies of the TMO_6 octahedra (TM = Mn, Cu). (c) SEM micrograph of as-synthesised $\text{Na}_{0.67}\text{Mn}_{0.9}\text{Cu}_{0.1}\text{O}_2$. (d) EDS mapping of $\text{Na}_{0.67}\text{Mn}_{0.9}\text{Cu}_{0.1}\text{O}_2$ showing the distribution of Na, Mn, Cu and O.

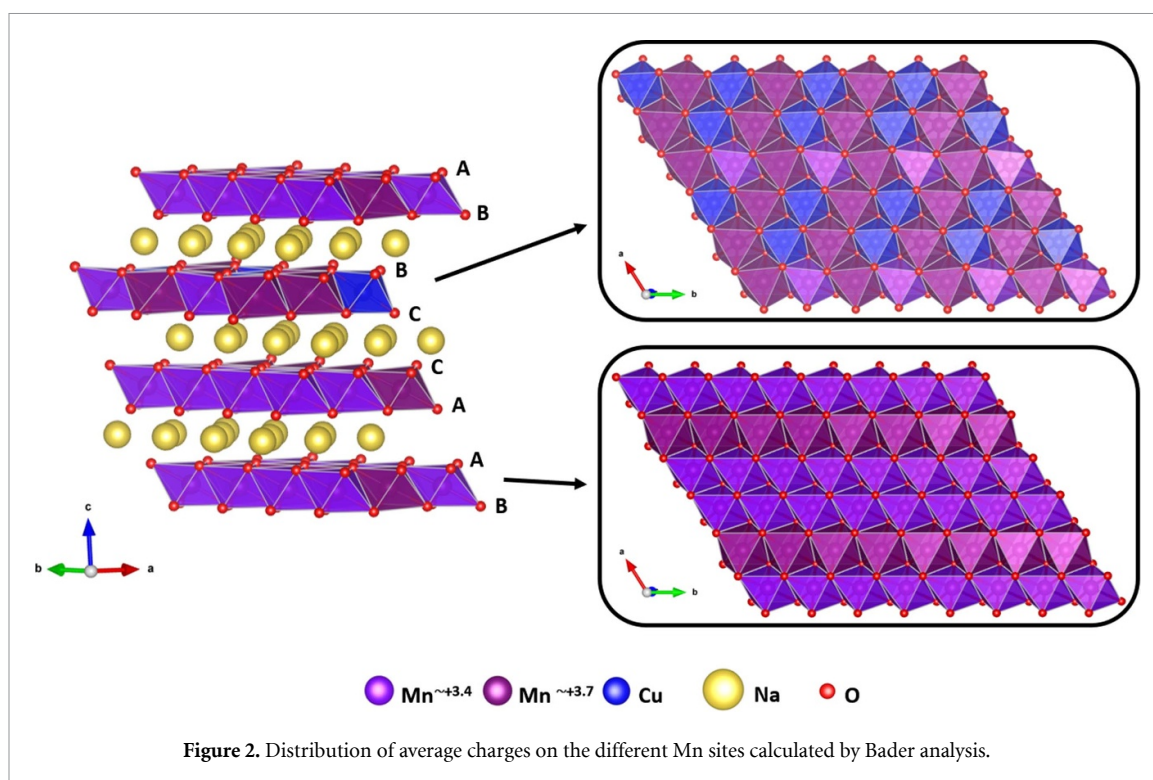
Table 1. Rietveld refinement results of as-synthesised $\text{Na}_{0.67}\text{Mn}_{0.9}\text{Cu}_{0.1}\text{O}_2$.

P3 $\text{Na}_x\text{Mn}_{0.9}\text{Cu}_{0.1}\text{O}_2$ synthesised in air						
R_{exp} : 3.04%, R_{wp} : 4.03%						
Lattice parameters P3 Space group $R3m$, $a = 2.8937(2)$ Å, $c = 16.869(3)$ Å						
Atom	Wyckoff symbol	x/a	y/b	z/c	Occupancy	Biso
Mn1/Cu1	3a	0	0	0	0.9/0.1	0.3
Na1	3a	0	0	0.1716(5)	0.69(1)	1.2
O1	3a	0	0	0.3834(8)	1	0.5
O2	3a	0	0	0.6014(10)	1	0.5

compensates for the charge deficit on this layer. The charge distribution on the other layers seems to be more favourable to Mn^{3+} by a factor of 2 (2 rows of $\text{Mn} \sim +3.4$ following a row of $\text{Mn} \sim +3.7$ in figure 2 for layer AB). It is noteworthy that in Bader charge analysis, the charge on an atom is the total charge present within each atom's atomic volume (Bader volume) [35]. It is often why this method does not accurately reproduce electrostatic potentials and dipole moments as it retains only atomic charges. This is therefore more to be considered as a qualitative tool than as a means of precisely calculating the charges on the different atoms.

3.2. Electrochemical properties of $\text{Na}_{0.67}\text{Mn}_{0.9}\text{Cu}_{0.1}\text{O}_2$

Sodium-half cells of $\text{Na}_{0.67}\text{Mn}_{0.9}\text{Cu}_{0.1}\text{O}_2$ were assembled and cycled galvanostatically between the voltage ranges 1.8–3.8 V and 1.8–4.3 V, at current rates of 10 mA g^{-1} and 100 mA g^{-1} . Figures 3(a) and (b) show the galvanostatic cycling performance of $\text{Na}_{0.67}\text{Mn}_{0.9}\text{Cu}_{0.1}\text{O}_2$ cycled between 1.8–3.8 V and 1.8–4.3 V, respectively. $\text{Na}_{0.67}\text{Mn}_{0.9}\text{Cu}_{0.1}\text{O}_2$ exhibits excellent cycling performance when cycled between 1.8 and 3.8 V (figure 3(a)), retaining 90% of its initial discharge capacity (166 and 158 mA h g^{-1}) over 40 cycles at 10 and 100 mA g^{-1} , respectively. Between 1.8 and 4.3 V (figure 3(b)), the extended voltage range resulted in a greater initial discharge capacity (195 mA h g^{-1}) attributed to oxygen anion redox (discussed later) but showed reduced cycling stability. At the slower rate of 10 mA h g^{-1} , $\text{Na}_{0.67}\text{Mn}_{0.9}\text{Cu}_{0.1}\text{O}_2$ maintains only 71% of the initial discharge capacity after 40 cycles. These results are comparable to P3-type $\text{Na}_{0.67}\text{Mn}_{0.8}\text{Ni}_{0.2}\text{O}_2$, whose cycling performance deteriorates on charging beyond 3.8 V [17]. The origin of this capacity loss may



be the partial transition to the O3-type phase due to the removal of more Na⁺ ions on charging (0.43 Na⁺ ions removed on first charge corresponding to 112 mA h g⁻¹), as revealed by *ex-situ* PXRD analysis (discussed later). At the faster rate of 100 mA g⁻¹, Na_{0.67}Mn_{0.9}Cu_{0.1}O₂ provides a reduced initial discharge capacity of 176 mA h g⁻¹ but better capacity retention of 83% after 40 cycles. It is reasonable to assume that on cycling at the faster rate (100 mA g⁻¹), that there are a lower O3 phase fraction and fewer side-reactions compared to cycling at 10 mA g⁻¹.

Figure 3(c) presents the differential capacity versus voltage (dQ/dV) plot for Na_{0.67}Mn_{0.9}Cu_{0.1}O₂ cycled over the voltage range 1.8–3.8 V. It reveals reversible redox couples, with oxidation peaks at 2.90, 3.16 and 3.51 V and broad reduction peaks at 2.79, 3.10 and 3.49 V. Over the extended voltage window of 1.8–4.3 V, figure 3(d) reveals an additional reversible redox couple, with an oxidation peak at 4.3 V and corresponding reduction peak at 4.19 V, attributed to oxygen anion redox. This process shows a relatively small voltage hysteresis of 110 mV for anionic redox. Furthermore, the intensity of this redox couple diminishes on cycling (highlighted in the inset), contributing somewhat to the capacity fade observed in figure 3(b).

The galvanostatic charge/discharge voltage profiles of Na_{0.67}Mn_{0.9}Cu_{0.1}O₂ cycled between 1.8–3.8 V and 1.8–4.3 V at 10 mA g⁻¹ over the first cycle and continued cycling are compared in figures 3(e) and S2, respectively. On first charge to 3.8 V, a charge capacity of 45 mA h g⁻¹ is delivered (corresponding to the removal of 0.18 Na⁺ ions), compensated by a combination of the oxidation of residual Mn³⁺ ions to Mn⁴⁺ ions (assuming the average Mn oxidation state is +3.43 derived from Rietveld refinement (table 1)) and oxidation of Cu²⁺ ions to Cu³⁺ ions (capable of delivering 26 mA h g⁻¹). On subsequent charge to 4.3 V, a further 67 mA h g⁻¹ was delivered (corresponding to the removal of 0.25 Na⁺ ions), attributed in part to electrolyte decomposition and oxygen anion redox. Upon discharge, smooth load curves are observed due to the dilution of the Jahn–Teller active Mn³⁺ ions by substitution of Cu²⁺ ions [36, 37], with extended plateaus at around 2.1 V associated with the Mn³⁺/Mn⁴⁺ redox couple.

Cyclic voltammograms were collected at a scan rate of 30 μV s⁻¹ from open-circuit voltage (OCV) to progressively higher positive potentials of 3.3 V, 3.8 V, and 4.3 V, fixing the lower voltage cut-off potential at 1.8 V for each cycle. The cyclic voltammograms for Na_{0.67}Mn_{0.9}Cu_{0.1}O₂ are shown in figure 3(e). Upon charging Na_{0.67}Mn_{0.9}Cu_{0.1}O₂ from OCV to 3.3 V and then discharging to 1.8 V, three reduction peaks are observed at 2.09, 2.02 and 2.44 V. On subsequent cycling, two oxidation peaks are observed at 2.23 and 2.34 V, coupled with the reduction peaks at 2.10 and 2.20 V, consistent with the Mn³⁺/Mn⁴⁺ redox couple. On the third cycle, an oxidation peak at 4.12 V is observed without any corresponding reduction peak, and a second oxidation peak at 4.23 V coupled to a reduction peak at 4.19 V and a second smaller, broad reduction peak at around 3.0 V, arising from oxygen redox associated with Cu doping. The irreversible oxidation peak at 4.12 V may be

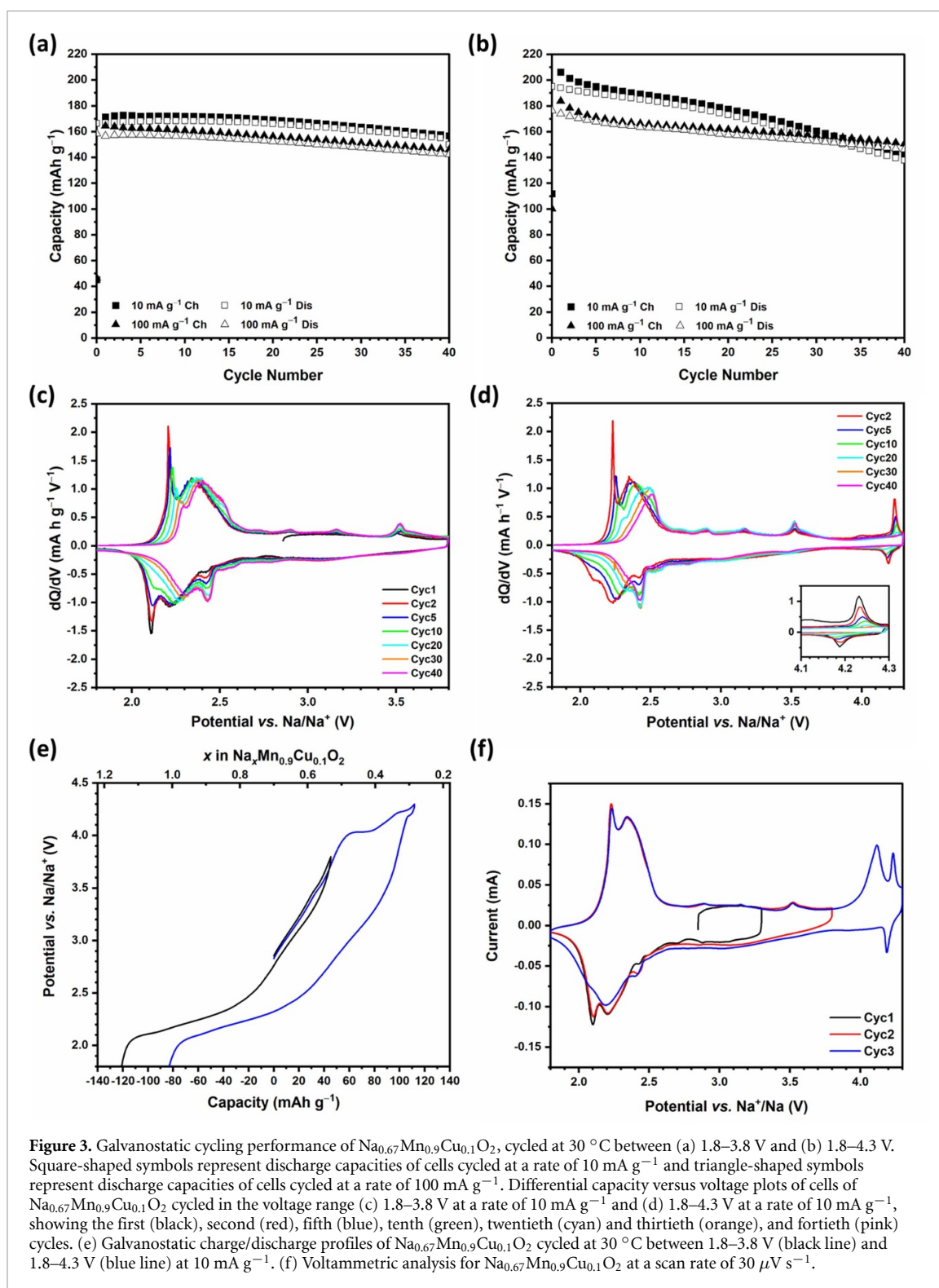
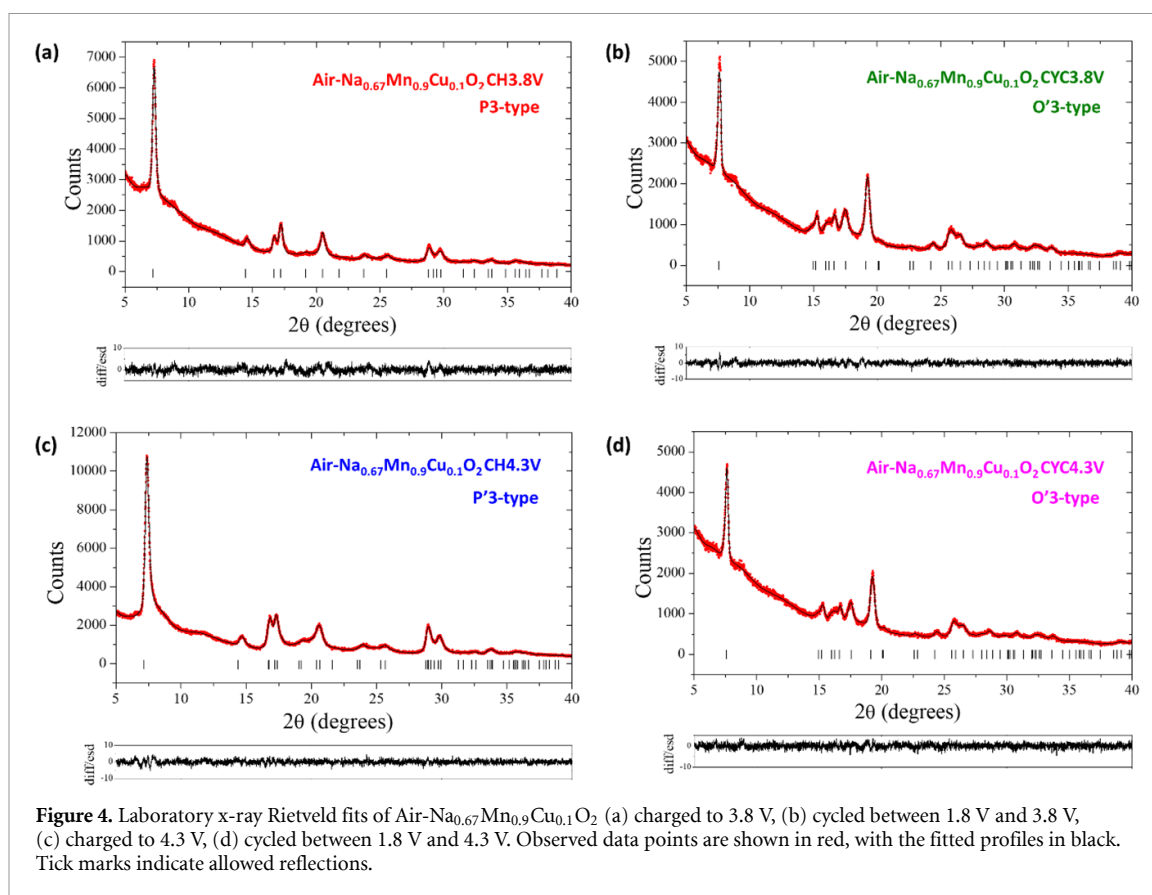


Figure 3. Galvanostatic cycling performance of $\text{Na}_{0.67}\text{Mn}_{0.9}\text{Cu}_{0.1}\text{O}_2$, cycled at 30 °C between (a) 1.8–3.8 V and (b) 1.8–4.3 V. Square-shaped symbols represent discharge capacities of cells cycled at a rate of 10 mA g⁻¹ and triangle-shaped symbols represent discharge capacities of cells cycled at a rate of 100 mA g⁻¹. Differential capacity versus voltage plots of cells of $\text{Na}_{0.67}\text{Mn}_{0.9}\text{Cu}_{0.1}\text{O}_2$ cycled in the voltage range (c) 1.8–3.8 V at a rate of 10 mA g⁻¹ and (d) 1.8–4.3 V at a rate of 10 mA g⁻¹, showing the first (black), second (red), fifth (blue), tenth (green), twentieth (cyan) and thirtieth (orange), and fortieth (pink) cycles. (e) Galvanostatic charge/discharge profiles of $\text{Na}_{0.67}\text{Mn}_{0.9}\text{Cu}_{0.1}\text{O}_2$ cycled at 30 °C between 1.8–3.8 V (black line) and 1.8–4.3 V (blue line) at 10 mA g⁻¹. (f) Voltammetric analysis for $\text{Na}_{0.67}\text{Mn}_{0.9}\text{Cu}_{0.1}\text{O}_2$ at a scan rate of 30 μV s⁻¹.

associated with decomposition of Na_2CO_3 [38]. The redox process centred around 4.20 V is consistent with the participation of oxygen anions in the charge compensation mechanism.

3.3. Structural evolution of $\text{Na}_{0.67}\text{Mn}_{0.9}\text{Cu}_{0.1}\text{O}_2$

The structural changes of $\text{Na}_{0.67}\text{Mn}_{0.9}\text{Cu}_{0.1}\text{O}_2$ upon Na^+ ion extraction/insertion were investigated by ex-situ PXRD. Electrodes of $\text{Na}_{0.67}\text{Mn}_{0.9}\text{Cu}_{0.1}\text{O}_2$ were cycled to various states of charge and discharge (figure S2), and PXRD patterns were collected. Rietveld refinements were carried out, and the fits are shown in figure 4. The refined structural parameters are detailed in table S1. Upon Na^+ ion extraction, the PXRD pattern of $\text{Na}_{0.67}\text{Mn}_{0.9}\text{Cu}_{0.1}\text{O}_2$ after being charged to 3.8 V (CH3.8 V, figure 4(a)) was fitted in the $R3m$ space group, suggesting that the P3-type structure was preserved. In addition, the data analyses demonstrate that



the a and c unit cell parameters contract and expand, respectively. The reduction along the a unit cell parameter relative to the pristine phase is consistent with the oxidation of residual Mn^{3+} to Mn^{4+} ions. The expansion of the c unit cell parameter arises because of increased Coulombic repulsion upon Na^+ ion extraction. At the end of charge (CH4.3V, figure 4(c)), the PXRD pattern reveals that the P3-type structure undergoes a distortion to P'3 structure and was fitted in the space group $C2/m$. Furthermore, figure 4(c) shows broader, asymmetric diffraction peaks suggestive of O-type stacking faults. Similar structural distortions ($\text{P3} \rightarrow \text{P}'3$) have been observed for P3-type Mg- and Zn-substituted counterparts after being charged to 4.3 V [26, 39]. It should be noted that upon initial charge to 4.3 V, more Na^+ ions (0.43 Na) are extracted from $\text{Na}_{0.67}\text{Mn}_{0.9}\text{Cu}_{0.1}\text{O}_2$ compared with $\text{Na}_{0.67}\text{Mn}_{0.9}\text{Zn}_{0.1}\text{O}_2$ (0.35 Na) and $\text{Na}_{0.67}\text{Mn}_{0.9}\text{Mg}_{0.1}\text{O}_2$ (0.39 Na) thereby resulting in greater Coulombic repulsion. Additionally, Cu is redox active ($\text{Cu}^{2+}/\text{Cu}^{3+}$) and undergoes volumetric changes, unlike Mg^{2+} (0.72 Å) and Zn^{2+} (0.74 Å) which are redox inactive. As such it is assumed that Cu^{2+} (0.73 Å) is oxidised to Cu^{3+} (0.54 Å) upon charge, and therefore the volume of the CuO_6 octahedra contracts to a similar size to that of Mn^{4+}O_6 octahedra (0.53 Å). By contrast the volumes of the Mg^{2+}O_6 octahedra and Zn^{2+}O_6 octahedra remain constant upon cycling and greater than that of the Mn^{4+}O_6 octahedra, providing structural stability which mediates such structural distortions [40]. Furthermore, Cu^{2+} ions exhibit a Jahn-Teller effect and an associated distortion of Cu^{2+}O_6 octahedra, resulting in local distortions which Mg^{2+} and Zn^{2+} do not exhibit.

Upon Na^+ ion insertion, the PXRD patterns of $\text{Na}_{0.67}\text{Mn}_{0.9}\text{Cu}_{0.1}\text{O}_2$ discharged to 1.8 V after charge to 3.8 V (CYC3.8 V) and 4.3 V (CYC4.3 V), figures 4(d) and (e), respectively, demonstrate a transformation to the O'3 phase. Transformation from the P3 phase to O'3 phase occurs to alleviate the Coulombic repulsion between the Na and Mn cations upon Na^+ ion insertion [41]. The phase transformation ($\text{P3} \rightarrow \text{P}'3$) and O-type stacking faults present after charging to 4.3 V, accompanied by the phase transformation ($\text{P3} \rightarrow \text{O}'3$) upon complete discharge likely contribute towards the observed capacity fade upon cycling (figure 3(b)).

3.4. Evolution of electronic structure

The charge compensation mechanism of $\text{Na}_{0.67}\text{Mn}_{0.9}\text{Cu}_{0.1}\text{O}_2$ upon Na^+ ion extraction/insertion was studied by means of SXAS and RIXS. Spectra were collected at the Mn and Cu L-edges, as well as O K-edge on ex-situ electrodes of $\text{Na}_{0.67}\text{Mn}_{0.9}\text{Cu}_{0.1}\text{O}_2$ extracted at the end of charge and discharge, cycled between two voltages 1.8–3.8 V and 1.8–4.3 V (figure S2). The Mn $L_{2,3}$ -edge SXAS were measured in the bulk sensitive PFY mode probing to depths deeper than 100 nm [42], and these spectra are shown in figure 5(a). To examine more

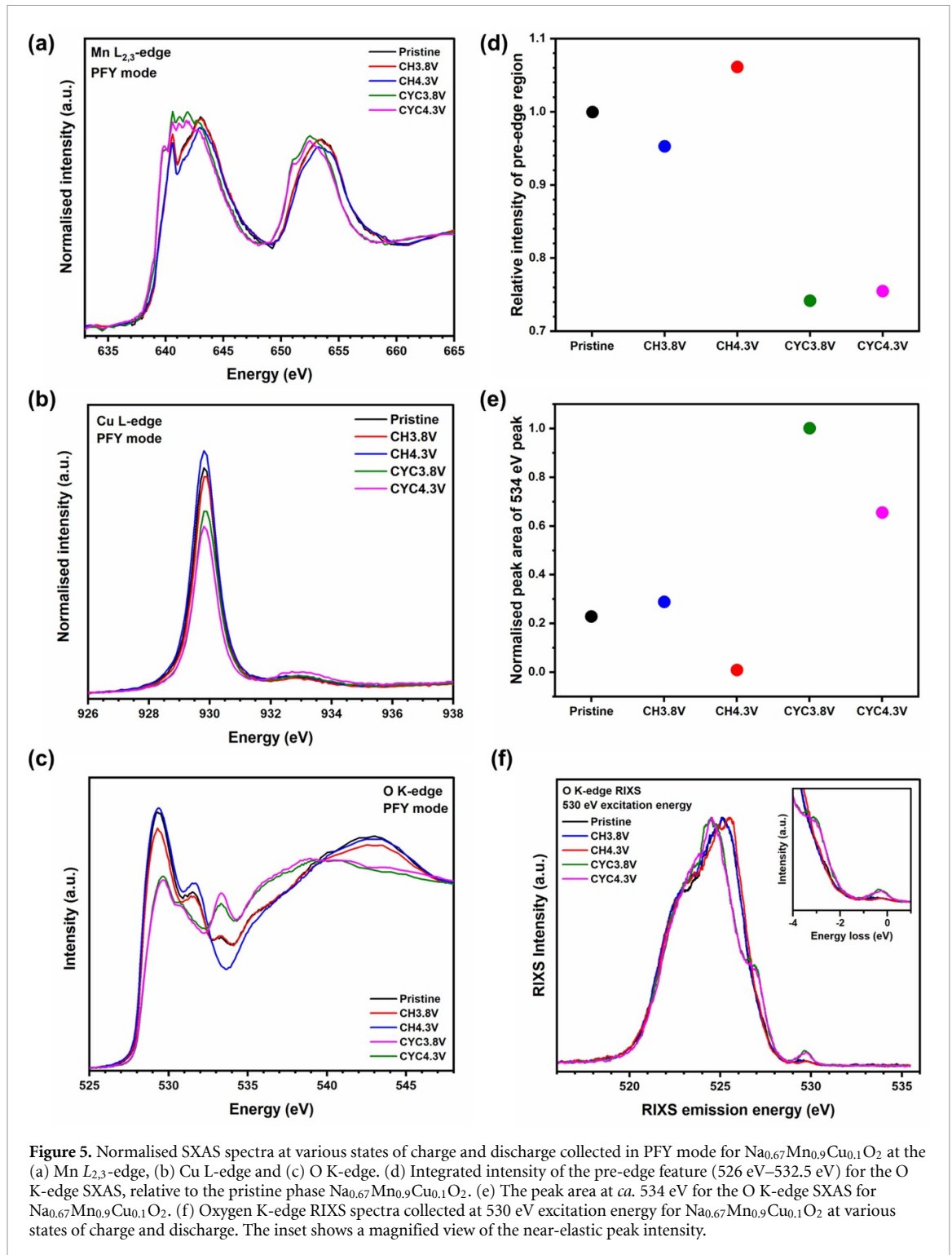


Figure 5. Normalised SXAS spectra at various states of charge and discharge collected in PFY mode for $\text{Na}_{0.67}\text{Mn}_{0.9}\text{Cu}_{0.1}\text{O}_2$ at the (a) Mn $L_{2,3}$ -edge, (b) Cu L-edge and (c) O K-edge. (d) Integrated intensity of the pre-edge feature (526 eV–532.5 eV) for the O K-edge SXAS, relative to the pristine phase $\text{Na}_{0.67}\text{Mn}_{0.9}\text{Cu}_{0.1}\text{O}_2$. (e) The peak area at ca. 534 eV for the O K-edge SXAS for $\text{Na}_{0.67}\text{Mn}_{0.9}\text{Cu}_{0.1}\text{O}_2$. (f) Oxygen K-edge RIXS spectra collected at 530 eV excitation energy for $\text{Na}_{0.67}\text{Mn}_{0.9}\text{Cu}_{0.1}\text{O}_2$ at various states of charge and discharge. The inset shows a magnified view of the near-elastic peak intensity.

closely the changes in energy upon charge/discharge, a Gaussian curve was fitted to the L_2 peak of each Mn PFY spectrum to determine the energy of the centre of the L_2 peak. Figure S4(a) reveals the change in energy of the L_2 peak upon charge/discharge. The Mn $L_{2,3}$ -edge of pristine $\text{Na}_{0.67}\text{Mn}_{0.9}\text{Cu}_{0.1}\text{O}_2$ exhibits a signature which is predominantly characteristic of Mn^{4+} , with some contributions from Mn^{3+} . Upon Na^+ ion extraction, figure S4(a) shows a slight increase in energy of the centre of the L_2 peak relative to the pristine material. This is consistent with the oxidation of residual Mn^{3+} ions to Mn^{4+} upon charging. These data indicate that there are only minor contributions from Mn ions in the charge compensation mechanism upon charge to 4.3 V. On subsequent discharge to 1.8 V after charge to 4.3 V, the Mn $L_{2,3}$ -edge spectra present signatures which are typical of Mn^{3+} . Figure S4(a) shows a decrease in the edge energy relative to the pristine material which indicates a reduction of Mn^{4+} to Mn^{3+} , showing the participation of $\text{Mn}^{3+}/\text{Mn}^{4+}$ redox

couple below 3.8 V. The SXAS spectra of the Mn L-edge in the surface sensitive TEY mode with a probing depth of 5 nm, indicates the formation of Mn^{2+} at the surface after discharge to 1.8 V (figure S4(b)).

Cu L_3 -edge SXAS spectra are shown in figure 5(b). The L_3 spectra show an intense absorption peak at 929.8 eV which relates to Cu^{2+} with transitions from the ground state $\text{Cu}(2p_{3/2})3d^9$ to the excited state $\text{Cu}(2p_{3/2})^{-1}3d^{10}$, where $(2p_{3/2})^{-1}$ represents a $2p_{3/2}$ hole [43–45]. After charge to 3.8 V, the intensity of the absorption peak at 929.8 eV increases relative to the pristine material and also broadens slightly. The broadening of the absorption peak at 929.8 eV upon Na^+ ion extraction can be reasonably attributed to partial oxidation of Cu^{2+} to Cu^{3+} and can be associated with transitions from $\text{Cu}(2p_{3/2})3d^9 \underline{L}$ ground state to $\text{Cu}(2p_{3/2})^{-1}3d^{10} \underline{L}$ excited state, where \underline{L} represents a ligand hole in the $2p$ orbital. Upon discharge, the intensity of this absorption peak decreases significantly and narrows considerably, demonstrating the reduction of Cu^{3+} to Cu^{2+} and hence reversibility of the process. In addition, this absorption peak remains essentially unshifted in energy upon cycling, thereby demonstrating that there are no changes in the energy of the half-occupied HOMO, suggesting that the coordination geometry of the CuO_6 octahedra is unchanged [46]. The spectra also reveal a small peak at ~ 932.9 eV which shows essentially no changes, this is consistent with a metal to ligand charge transfer feature and has been verified in previous reports [47, 48]. The O K-edge SXAS spectra were collected to study the contribution of oxygen to the charge compensation mechanism and the data are shown in figure 5(c). Below 533 eV, the spectra reveal absorption peaks at *ca.* 530 and 532 eV which relate to electronic transitions from the O $1s$ states to unoccupied hybridised O $2p$ -TM t_{2g} and O $2p$ -TM e_g states, respectively. The integral of these absorption peaks between 526–534.3 eV, corresponds to changes in the density of empty states above the Fermi level. The evolution of these changes in the area beneath the absorption peaks, relative to the pristine material is shown in figure 5(d). Upon Na^+ ion extraction, figure 5(d) shows small variations of the integral, corresponding to the hybridisation of the O $2p$ and TM $3d$ states. After charge to 4.3 V, the intensity increases which suggests that electrons are removed from oxygen, indicative of oxygen anion redox. At the end of discharge to 1.8 V, the intensity decreases significantly relative to pristine $\text{Na}_{0.67}\text{Mn}_{0.9}\text{Cu}_{0.1}\text{O}_2$, suggesting that the electron-holes of the oxygen $2p$ states are refilled, as well as a reduction of Mn^{4+} to Mn^{3+} which is consistent with the Mn K-edge data (figure 5(a)). These data also demonstrate the reversibility of the oxygen redox reaction figure 5(c) also reveals changes in the absorption peak at 534 eV, associated with the unoccupied O $2p$ states hybridised with Na $3d$ states [49–51]. Figure 5(e) shows the area of the *ca.* 534 eV absorption peak as a function of charge/discharge. The peak intensity decreases upon charging to higher voltages (i.e. Na^+ ion extraction), reaching a minimum after charge to 4.3 V and then increases after discharge to 1.8 V (i.e. Na^+ ion insertion), showing that this trend matches the level of sodiation (figure S2). These data are analogous to those observed for Zn-substituted P3- $\text{Na}_{0.67}\text{Mn}_{0.9}\text{Zn}_{0.1}\text{O}_2$ [26].

In figure 5(f) O K-edge RIXS excited at the main resonance is shown revealing that additional spectral weight builds up upon charge: first at around 524 eV when charging from pristine to 3.8 V and then also at 526.1 eV when further charged to 4.3 V. Upon discharge to 1.8 V the main peak shifts significantly to lower energy, thereby narrowing the entire O $2p$ band. A new shoulder at the high energy side is associated with hybridisation of Mn $3d$ states with oxygen states reflecting the refilling of the (more localised) Mn $3d$ band upon re-sodiation. Note that in contrast to the main peak, the latter feature tracks the elastic peak energy at a constant energy difference, which is expected for such localised excitations. The inset of figure 5(f) shows the near-elastic peak region, corroborating the increased localisation in the discharged state as well as oxygen state evolution during the charging process.

3.5. Comparison of divalent dopants

To explore more in-depth the nature of the oxygen anion redox activity observed in P3 type $\text{Na}_{0.67}\text{Mn}_{0.9}\text{Cu}_{0.1}\text{O}_2$, DFT calculations were performed. Based on the pDOS, shown in figure 6(a), the contribution from O $2p$ states at the highest occupied states around the Fermi level (highlighted in yellow in figure 6(a)) is significant, and slightly overlaps with the Cu e_g orbital. This suggests that the O $2p$ orbital exhibits strong orbital hybridisation with the Cu e_g orbital at the Fermi level [27, 52]. Therefore, the strong covalent Cu–O bonds in P3- $\text{Na}_{0.67}\text{Mn}_{0.9}\text{Cu}_{0.1}\text{O}_2$ are likely to be the redox-active centre in the electrochemical process.

We extended our study on P3- $\text{Na}_{0.67}\text{Mn}_{0.9}\text{Cu}_{0.1}\text{O}_2$ and compared its electrochemical performance with Mg- and Zn-substituted $\text{Na}_{0.67}\text{Mn}_{0.9}\text{M}_{0.1}\text{O}_2$ ($M = \text{Cu}, \text{Mg}, \text{Zn}$). These materials were synthesised using the same co-precipitation method and heated under air at 625 °C. The PXRD patterns of as-synthesised $\text{Na}_{0.67}\text{Mn}_{0.9}\text{M}_{0.1}\text{O}_2$ ($M = \text{Cu}, \text{Mg}, \text{Zn}$) are compared in figure S5. The major diffraction peaks of the PXRD patterns of all samples can be indexed using the P3 structure with $R3m$ space group. Figure 6(b) shows the charge/discharge profiles of the three materials cycled within the voltage range 1.8–4.3 V at 10 mA g^{-1} for the first cycle. The Mg- and Zn-substituted materials behave in an analogous manner to the Cu-substituted phase, exhibiting oxygen anion redox activity over the high-voltage region. $\text{Na}_{0.67}\text{Mn}_{0.9}\text{Cu}_{0.1}\text{O}_2$ reaches a

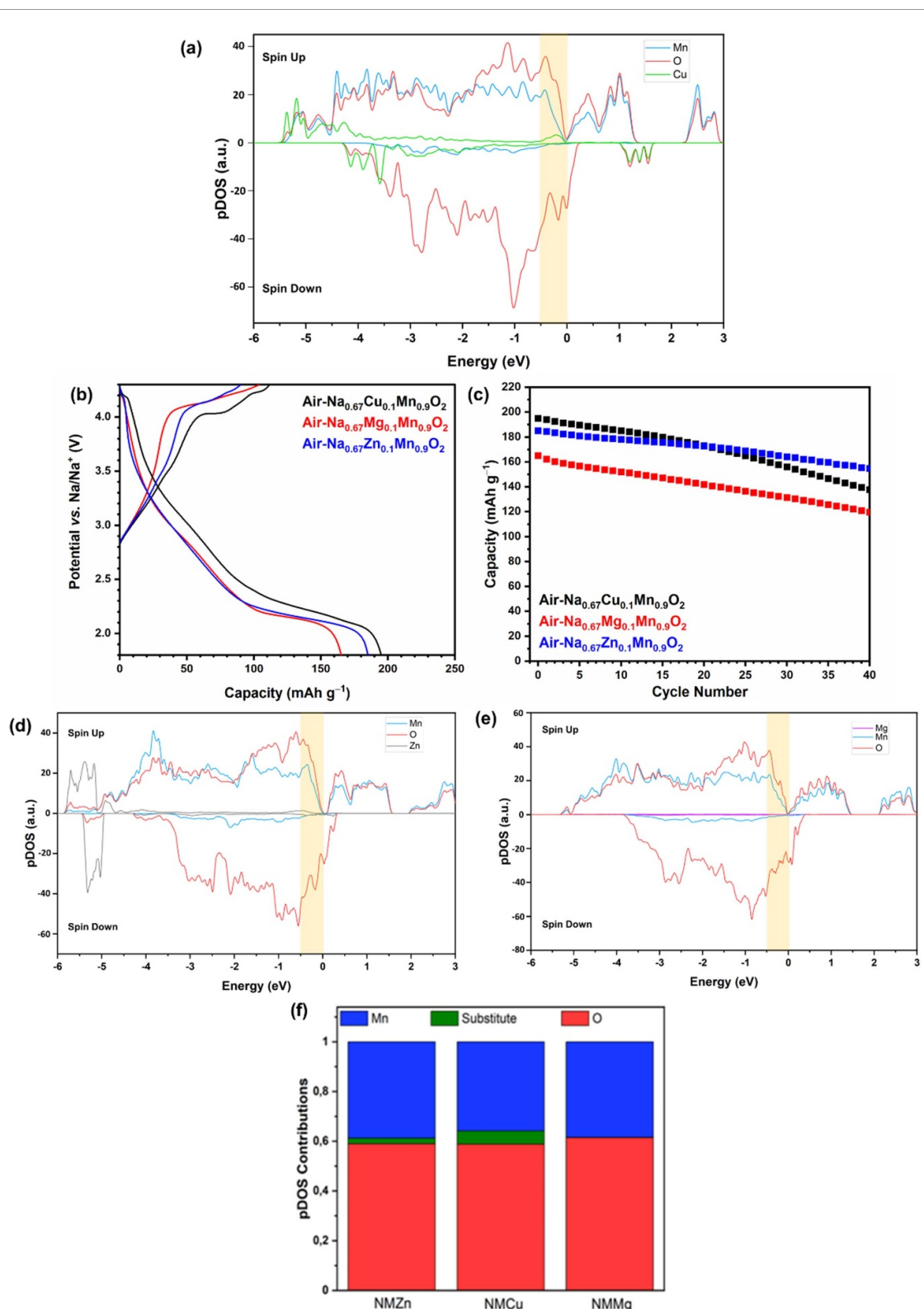


Figure 6. (a) Calculated pDOS of P3-Na_{0.67}Mn_{0.9}Cu_{0.1}O₂ (NMCu), with the yellow highlighted region (-0.5–0 eV) corresponding to the highest occupied states just below the Fermi level. (b) Comparison of electrochemical properties of Na_{0.67}Mn_{0.9}Cu_{0.1}O₂ (black), Na_{0.67}Mn_{0.9}Mg_{0.1}O₂ (red) and Na_{0.67}Mn_{0.9}Zn_{0.1}O₂ (blue) showing the charge/discharge profiles for the first cycle and (c) galvanostatic cycling performance showing the discharge capacities of half-cells cycled at 30 °C between 1.8–4.3 V at a rate of 10 mA g⁻¹. Calculated pDOS for (d) P3-Na_{0.67}Mn_{0.9}Zn_{0.1}O₂ (NMZn) and (e) P3-Na_{0.67}Mn_{0.9}Mg_{0.1}O₂ (NMMg). (f) Schematic diagrams of pDOS contributions of both TM and O within the structures NMZn, NMCu and NMMg. Values are integrated just below the Fermi level between -0.5 eV and 0 eV.

greater charge/discharge capacity due in part to the Cu²⁺/Cu³⁺ redox reaction which can provide an additional theoretical capacity of 26 mA h g⁻¹ compared to the Mg- and Zn-substituted materials since Mg²⁺ and Zn²⁺ are redox inactive, as well as presenting enhanced oxygen anion redox. In addition, the

cycling performances of the three materials are compared in figure 6(c). Cu-substituted $\text{Na}_{0.67}\text{Mn}_{0.9}\text{Cu}_{0.1}\text{O}_2$ shows a greater initial discharge capacity of 195 mA h g^{-1} , but its capacity deteriorates after 20 cycles, showing a capacity loss of 29% after 40 cycles, attributed to the structural instability of $\text{Na}_{0.67}\text{Mn}_{0.9}\text{Cu}_{0.1}\text{O}_2$, as discussed above. As for $\text{Na}_{0.67}\text{Mn}_{0.9}\text{Mg}_{0.1}\text{O}_2$, it shows a reduced initial discharge capacity of 165 mA h g^{-1} and maintains only 72% of its initial capacity after 40 cycles. Whereas the Zn-substituted material, $\text{Na}_{0.67}\text{Mn}_{0.9}\text{Zn}_{0.1}\text{O}_2$ shows a reduced initial discharge capacity of 185 mA h g^{-1} compared to the Cu-substituted material but reveals enhanced cycling performance, retaining 84% of its initial discharge capacity after 40 cycles. Comparatively, based on earlier structural studies of P3- $\text{Na}_{0.67}\text{Mn}_{0.9}\text{M}_{0.1}\text{O}_2$ ($M = \text{Zn, Mg}$) [26, 39], the substitution of Mn by Zn provides a more stable framework for Na^+ ion insertion/extraction than substitution by Mg or Cu. These data are consistent with O3- $\text{NaNi}_{0.45}\text{M}_{0.5}\text{Mn}_{0.4}\text{Ti}_{0.1}\text{O}_2$ (where $M = \text{Mg, Zn, Cu}$) which similarly showed that the Zn-substituted material displayed superior cycling stability [53].

To further investigate the nature of the oxygen anion redox activity observed for P3- $\text{Na}_{0.67}\text{Mn}_{0.9}\text{M}_{0.1}\text{O}_2$ ($M = \text{Cu, Mg, Zn}$), additional DFT calculations were carried out. Figures 6(d) and (e) show the pDOS of P3-type $\text{Na}_{0.67}\text{Mn}_{0.9}\text{Zn}_{0.1}\text{O}_2$ (NMZn) and $\text{Na}_{0.67}\text{Mn}_{0.9}\text{Mg}_{0.1}\text{O}_2$ (NMMg), respectively. The integrated pDOS between -0.5 eV and 0 eV was used to estimate how much a given band element dominates just below the Fermi level and based on the schematic diagrams of pDOS contributions (figure 6(f)), we expect Cu-containing materials to have less oxygen-electron availability for redox than Zn and Mg during electrochemical cycling due to its more electronegative nature compared with Mg [54], or Zn [11]. But also, because of its non-filled $3d^9$ band, the occupancy of Cu e_g states next to the Fermi level allows the possibility of the $\text{Cu}^{2+}/\text{Cu}^{3+}$ redox reaction in addition to $\text{Mn}^{3+}/\text{Mn}^{4+}$ and $\text{O}^{2-}/(\text{O}_2)^{n-}$ redox couples.

These observations suggest that chemical substitution is an effective tool to trigger oxygen participation. The nature of the transition metal as well as the bond strength can play a significant role in enhancing the presence of O $2p$ states near the Fermi level.

4. Conclusions

P3-type Cu-substituted $\text{Na}_{0.67}\text{Mn}_{0.9}\text{Cu}_{0.1}\text{O}_2$ was investigated as a positive electrode material for SIBs. $\text{Na}_{0.67}\text{Mn}_{0.9}\text{Cu}_{0.1}\text{O}_2$ exhibits a highly reversible capacity of 138 mA h g^{-1} between the voltage range 1.8–3.8 V after 40 cycles. Over the voltage range 1.8–4.3 V, $\text{Na}_{0.67}\text{Mn}_{0.9}\text{Cu}_{0.1}\text{O}_2$ presents a greater initial capacity of $176.3 \text{ mA h g}^{-1}$, with the additional capacity arising from oxygen anion redox chemistry. The capacity fades (capacity retention of 71% after 40 cycles at 10 mA g^{-1}) over this extended voltage range and ex-situ PXRD reveals a distortion of the P3 phase to the P'3 phase after charge to 4.3 V and then a complete phase transformation of P'3→O'3 upon discharge to 1.8 V, contributing to the capacity loss. DFT calculations demonstrates the presence of strong covalency between Cu $3d$ and O $2p$ orbitals which facilitates the oxygen anion redox activity in this material.





Data availability statement

The data that support the findings of this study are available upon reasonable request from the authors.

Acknowledgments

The authors are grateful for the provision of beam time on BL27SU at Spring 8 (Proposal No. 2021A1425). We gratefully acknowledge technical support of the Spring 8 user support, particularly beamline scientist Kiyofumi Nitta. This work was supported by the Faraday Institution (Grant No. FIRG018). The authors gratefully acknowledge support from the Engineering and Physical Sciences Research Council (EPSRC), Grant Nos. EP/L017008/1, EP/R023751/1 and EP/T019298/1.

ORCID iDs

Stephanie F Linnell  <https://orcid.org/0000-0002-8462-2514>
Alexis G Manche  <https://orcid.org/0000-0002-8505-474X>
Moritz Hirsbrunner  <https://orcid.org/0000-0003-3931-6638>
Aaron B Naden  <https://orcid.org/0000-0003-2876-6991>
John T S Irvine  <https://orcid.org/0000-0002-8394-3359>
Laurent C Duda  <https://orcid.org/0000-0001-8471-0955>
A Robert Armstrong  <https://orcid.org/0000-0003-1937-0936>

References

- [1] Hwang J Y, Myung S T and Sun Y K 2017 Sodium-ion batteries: present and future *Chem. Soc. Rev.* **46** 3529–614
- [2] Yabuuchi N, Kubota K, Dahbi M and Komaba S 2014 Research development on sodium-ion batteries *Chem. Rev.* **114** 11636–82
- [3] Armand M and Tarascon J-M 2008 Building better batteries *Nature* **451** 652–7
- [4] Tapia-rui N et al 2021 2021 roadmap for sodium-ion batteries *J. Phys. Energy* **3** 031503
- [5] Li Y, Lu Y, Zhao C, Hu Y S, Titirici M M, Li H, Huang X and Chen L 2017 Recent advances of electrode materials for low-cost sodium-ion batteries towards practical application for grid energy storage *Energy Storage Mater.* **7** 130–51
- [6] Fang C, Huang Y, Zhang W, Han J, Deng Z, Cao Y and Yang H 2016 Routes to high energy cathodes of sodium-ion batteries *Adv. Energy Mater.* **6** 1–18
- [7] Do J, Kim I, Kim H and Jung Y 2020 Towards stable Na-rich layered transition metal oxides for high energy density sodium-ion batteries *Energy Storage Mater.* **25** 62–69
- [8] Rozier P, Sathiya M, Paulraj A R, Foix D, Desautay T, Taberna P L, Simon P and Tarascon J M 2015 Anionic redox chemistry in Na-rich $\text{Na}_2\text{Ru}_{1-y}\text{Sn}_y\text{O}_3$ positive electrode material for Na-ion batteries *Electrochem. Commun.* **53** 29–32
- [9] Mortemard De Boisse B et al 2016 Intermediate honeycomb ordering to trigger oxygen redox chemistry in layered battery electrode *Nat. Commun.* **7** 1–9
- [10] Mortemard de Boisse B, Reynaud M, Ma J, Kikkawa J, Nishimura S I, Casas-Cabanas M, Delmas C, Okubo M and Yamada A 2019 Coulombic self-ordering upon charging a large-capacity layered cathode material for rechargeable batteries *Nat. Commun.* **10** 2185
- [11] Maitra U et al 2018 Oxygen redox chemistry without excess alkali-metal ions in $\text{Na}_{2/3}[\text{Mg}_{0.28}\text{Mn}_{0.72}]\text{O}_2$ *Nat. Chem.* **10** 288–95
- [12] House R A et al 2020 Superstructure control of first-cycle voltage hysteresis in oxygen-redox cathodes *Nature* **577** 502–8
- [13] Liu Z et al 2021 Ultralow volume change of P2-type layered oxide cathode for Na-ion batteries with controlled phase transition by regulating distribution of Na^+ *Angew. Chem., Int. Ed.* **60** 20960–9
- [14] Gu Z, Guo J, Sun Z-H, Zhao X-X, Wang X-T, Liang H-J, Wu X-L and Liu Y 2021 Air/water/temperature-stable cathode for all-climate sodium-ion batteries for all-climate sodium-ion batteries *Cell Rep. Phys. Sci.* **2** 100665
- [15] Delmas C, Fouassier C and Hagenmuller P 1980 Structural classification and properties of the layered oxides *Physica B+C* **99** 81–85
- [16] Kumakura S, Tahara Y, Sato S, Kubota K and Komaba S 2017 P'2- $\text{Na}_{2/3}\text{Mn}_{0.9}\text{Me}_{0.1}\text{O}_2$ (Me = Mg, Ti, Co, Ni, Cu, and Zn): correlation between orthorhombic distortion and electrochemical property *Chem. Mater.* **29** 8958–62
- [17] Kim E J, Ma L A, Duda L C, Pickup D M, Chadwick A V, Younesi R, Irvine J T S and Robert Armstrong A 2020 Oxygen redox activity through a reductive coupling mechanism in the P3-type nickel-doped sodium manganese oxide *ACS Appl. Energy Mater.* **3** 184–91
- [18] Kim E J, Mofredj K, Pickup D M, Chadwick A V, Irvine J T S and Armstrong A R 2021 Activation of anion redox in P3 structure cobalt-doped sodium manganese oxide via introduction of transition metal vacancies *J. Power Sources* **481** 229010
- [19] Dai K, Mao J, Zhuo Z, Feng Y, Mao W, Ai G, Pan F, Chuang Y, Liu G and Yang W 2020 Negligible voltage hysteresis with strong anionic redox in conventional battery electrode *Nano Energy* **74** 104831
- [20] Hakim C, Sabi N, Ma L A, Dahbi M, Brandell D, Edström K, Duda L C, Saadouni I and Younesi R 2020 Understanding the redox process upon electrochemical cycling of the P2- $\text{Na}_{0.78}\text{Co}_{1/2}\text{Mn}_{1/3}\text{Ni}_{1/6}\text{O}_2$ electrode material for sodium-ion batteries *Commun. Chem.* **3** 9
- [21] Ma C, Alvarado J, Xu J, Clément R J, Kodur M, Tong W, Grey C P and Meng Y S 2017 Exploring oxygen activity in the high energy P2-type $\text{Na}_{0.78}\text{Ni}_{0.23}\text{Mn}_{0.69}\text{O}_2$ cathode material for Na-ion batteries *J. Am. Chem. Soc.* **139** 4835–45
- [22] Konarov A, Kim H J, Jo J, Voronina N, Lee Y, Bakenov Z, Kim J and Myung S 2020 High-voltage oxygen-redox-based cathode for rechargeable sodium-ion batteries *Adv. Energy Mater.* **10** 2001111
- [23] Carlier D, Cheng J H, Berthelot R, Guignard M, Yoncheva M, Stoyanova R, Hwang B J and Delmas C 2011 The P2- $\text{Na}_{2/3}\text{Co}_{2/3}\text{Mn}_{1/3}\text{O}_2$ phase: structure, physical properties and electrochemical behavior as positive electrode in sodium battery *Dalton Trans.* **40** 9306–12
- [24] Zheng W, Liu Q, Wang Z, Wu Z, Gu S, Cao L, Zhang K, Fransaer J and Lu Z 2020 Oxygen redox activity with small voltage hysteresis in $\text{Na}_{0.67}\text{Cu}_{0.28}\text{Mn}_{0.72}\text{O}_2$ for sodium-ion batteries *Energy Storage Mater.* **28** 300–6
- [25] Talaie E, Kim S Y, Chen N and Nazar L F 2017 Structural evolution and redox processes involved in the electrochemical cycling of P2- $\text{Na}_{0.67}[\text{Mn}_{0.66}\text{Fe}_{0.20}\text{Cu}_{0.14}]\text{O}_2$ *Chem. Mater.* **29** 6684–97
- [26] Linnell S F, Hirsbrunner M, Imada S, Cibin G, Naden A B, Chadwick A V, Irvine J T S, Duda L C and Armstrong A R 2022 Enhanced cycling stability in the anion redox material P3-type Zn-substituted sodium manganese oxide *ChemElectroChem* **9** e202200240
- [27] Wang P F et al 2020 Both cationic and anionic redox chemistry in a P2-type sodium layered oxide *Nano Energy* **69** 104474
- [28] Mason C W, Lange F, Saravanan K, Lin F and Nordlund D 2015 Beyond divalent copper: a redox couple for sodium ion battery cathode materials *ECS Electrochem. Lett.* **4** A41
- [29] Kang W, Yu D Y W, Lee P K, Zhang Z, Bian H, Li W, Ng T W, Zhang W and Lee C S 2016 P2-type $\text{Na}_x\text{Cu}_{0.15}\text{Ni}_{0.20}\text{Mn}_{0.65}\text{O}_2$ cathodes with high voltage for high-power and long-life sodium-ion batteries *ACS Appl. Mater. Interfaces* **8** 31661–8
- [30] Kang W, Zhang Z, Lee P K, Ng T W, Li W, Tang Y, Zhang W, Lee C S and Wai Y D Y 2015 Copper substituted P2-type $\text{Na}_{0.67}\text{Cu}_x\text{Mn}_{1-x}\text{O}_2$: a stable high-power sodium-ion battery cathode *J. Mater. Chem. A* **3** 22846–52
- [31] Coelho A A 2018 TOPAS and TOPAS-Academic: an optimization program integrating computer algebra and crystallographic objects written in C++ *J. Appl. Cryst.* **51** 210–8
- [32] Ohashi H, Ishiguro E, Tamenori Y, Kishimoto H, Tanaka M, Irie M, Tanaka T and Ishikawa T 2001 Outline of soft x-ray photochemistry beamline BL27SU of SPring-8 *Nucl. Instrum. Methods Phys. Res. A* **467–468** 529–32
- [33] Perdew J P, Burke K and Ernzerhof M 1996 Generalized gradient approximation made simple *Phys. Rev. Lett.* **77** 3865–8
- [34] Tang W, Sanville E and Henkelman G 2009 A grid-based Bader analysis algorithm without lattice bias *J. Phys.: Condens. Matter* **21** 084204
- [35] Henkelman G, Arnaldsson A and Jónsson H 2006 A fast and robust algorithm for Bader decomposition of charge density *Comput. Mater. Sci. Mater.* **36** 354–60
- [36] Billaud J, Singh G, Armstrong A R, Gonzalo E, Roddatis V, Armand M, Rojo T and Bruce P G 2014 $\text{Na}_{0.67}\text{Mn}_{1-x}\text{Mg}_x\text{O}_2$ ($0 \leq x \leq 0.2$): a high capacity cathode for sodium-ion batteries *Energy Environ. Sci.* **7** 1387–91
- [37] Wang P et al 2020 Elucidation of the Jahn–Teller effect in a pair of sodium isomer *Nano Energy* **77** 105167
- [38] Wang Q, Mariyappan S, Vergnet J, Abakumov A M, Rousse G, Rabuel F, Chakir M and Tarascon J M 2019 Reaching the energy density limit of layered O3- $\text{NaNi}_{0.5}\text{Mn}_{0.5}\text{O}_2$ electrodes via dual Cu and Ti substitution *Adv. Energy Mater.* **9** 1–11

- [39] Kim E J, Ma L A, Pickup D M, Chadwick A V, Younesi R, Maughan P, Irvine J T S and Armstrong A R 2020 Vacancy-enhanced oxygen redox reversibility in P3-type magnesium-doped sodium manganese oxide $\text{Na}_{0.67}\text{Mg}_{0.2}\text{Mn}_{0.8}\text{O}_2$ *ACS Appl. Energy Mater.* **3** 10423–34
- [40] Shannon R D 1976 Revised effective ionic radii and systematic studies of interatomic distances in halides and chalcogenides *Acta Cryst.* **A32** 751–67
- [41] Parant J-P, Olazcuaga R, Devalette M, Fouassier C and Hagemuller P 1971 Sur Quelques Nouvelles Phases de Formule Na_xMnO_2 ($x < 1$) *J. Solid State Chem.* **3** 1–11
- [42] Asakura D et al 2016 Material/element-dependent fluorescence-yield modes on soft x-ray absorption spectroscopy of cathode materials for Li-ion batteries *AIP Adv.* **6** 035105
- [43] Grioni M, van Acker J F, Czyzyk M T and Fuggle J C 1992 Unoccupied electronic structure and core-hole effects in the x-ray absorption spectra of Cu_2O *Phys. Rev. B* **45** 3309–18
- [44] Morita Y, Karpinen M, Yamauchi H, Liu R S and Chen J M 2003 XANES study on the evolution among different copper species, Cu^I , Cu^{II} , Cu^{III} , in $\text{CuBa}_2\text{YCu}_2\text{O}_{6+z}$ upon oxygen loading *J. Low Temp. Phys.* **131** 1205–10
- [45] Grioni M, Goedkoop J B, Schoorl R, de Groot F M F, Fuggle J C, Schäfers F, Koch E E, Rossi G, Esteva J-M and Karnatak R C 1989 Studies of copper valence states with Cu L_3 x-ray-absorption spectroscopy *Phys. Rev. B* **39** 1541–5
- [46] Baker M L, Mara M W, Yan J J, Hodgson K O, Hedman B and Solomon E I 2017 K- and L-edge x-ray absorption spectroscopy (XAS) and resonant inelastic x-ray scattering (RIXS) determination of differential orbital covalency (DOC) of transition metal sites *Coord. Chem. Rev.* **345** 182–208
- [47] Bonhommeau S, Pontius N, Cobo S, Salmon L, De Groot F M F, Molnár G, Bousseksou A, Dürr H A and Eberhardt W 2008 Metal-to-ligand and ligand-to-metal charge transfer in thin films of Prussian blue analogues investigated by x-ray absorption spectroscopy *Phys. Chem. Chem. Phys.* **10** 5882–9
- [48] Xu S et al 2018 Suppressing the voltage decay of low-cost P2-type iron-based cathode materials for sodium-ion batteries *J. Mater. Chem. A* **6** 20795–803
- [49] Wu W B, Huang D J, Okamoto J, Tanaka A, Lin H J, Chou F C, Fujimori A and Chen C T 2005 Orbital symmetry and electron correlation in Na_xCoO_2 *Phys. Rev. Lett.* **94** 146402
- [50] Kroll T, Knufer M, Geck J, Hess C, Schwieger T, Krabbes G, Sekar C, Batchelor D R, Berger H and Büchner B 2006 X-ray absorption spectroscopy of Na_xCoO_2 layered cobaltates *Phys. Rev. B* **74** 1–6
- [51] Hirsh H, Li Y, Cheng J-H, Shimizu R, Zhang M, Zhao E and Meng Y S 2021 The negative impact of transition metal migration on oxygen redox activity of layered cathode materials for Na-ion batteries *J. Electrochem. Soc.* **168** 040539
- [52] Assadi M H N, Okubo M, Yamada A and Tateyama Y 2018 Oxygen redox in hexagonal layered Na_xTMO_3 (TM = 4d elements) for high capacity Na-ion batteries *ACS Omega* **3** 12215–28
- [53] Mariyappan S, Marchandier T, Rabuel F, Iadecola A, Rousse G, Morozov A V, Abakumov A M and Tarascon J-M 2020 The role of divalent ($\text{Zn}^{2+}/\text{Mg}^{2+}/\text{Cu}^{2+}$) substituents in achieving full capacity of sodium layered oxides for Na-ion battery applications *Chem. Mater.* **32** 1657–66
- [54] Bai X, Sathiyar M, Mendoza-sánchez B, Iadecola A, Vergnet J, Dedryvère R, Saubanère M, Abakumov A M, Rozier P and Gerhardt I C 2018 Anionic redox activity in a newly Zn-doped sodium layered oxide $\text{P2-Na}_{2/3}\text{Mn}_{1-y}\text{Zn}_y\text{O}_2$ ($0 < y < 0.23$) *Adv. Energy Mater.* **8** 1802379